Phase-shifted $\mathcal{PT}$-symmetric periodic structures

S. Vignesh Raja,[1,*] A. Govindarajan,[2,†] A. Mahalingam,[1,‡] and M. Lakshmanan[2,§]
[1]*Department of Physics, Anna University, Chennai - 600 025, India*
[2]*Centre for Nonlinear Dynamics, School of Physics, Bharathidasan University, Tiruchirappalli - 620 024, India*

(Received 9 May 2020; accepted 7 July 2020; published 29 July 2020)

We report the spectral features of a phase-shifted parity and time ($\mathcal{PT}$) symmetric fiber Bragg grating and demonstrate its functionality as a demultiplexer in the unbroken $\mathcal{PT}$-symmetric regime. The length of the proposed system is of the order of millimeters and the lasing spectra in the broken $\mathcal{PT}$-symmetric regime can be easily tuned in terms of intensity, bandwidth, and wavelength by varying the magnitude of the phase shift in the middle of the structure. Surprisingly, the multimodal lasing spectra are suppressed by virtue of judiciously selected phase and the gain-loss value. Also, it is possible to obtain sidelobe-less spectra in the broken $\mathcal{PT}$-symmetric regime without a need for an apodization profile, which is a traditional way to tame the unwanted sidelobes. The system is found to show narrow-band single-mode lasing behavior for a wide range of phase-shift values for given values of gain and loss. Moreover, we report the intensity-tunable reflection and transmission characteristics in the unbroken regime via variation in gain and loss. At the exceptional point, the system shows unidirectional wave transport phenomenon independent of the presence of phase shift in the middle of the grating. For the right light-incidence direction, the system exhibits zero reflection wavelengths within the stopband at the exceptional point. We also investigate the role of multiple phase shifts placed at fixed locations along the length of the FBG and the variations in the spectra when the phase-shift and gain-loss values are tuned. In the broken $\mathcal{PT}$-symmetric regime, the presence of multiple phase shifts aids in controlling the number of reflectivity peaks besides controlling their magnitude. The advantage of the proposed model is that it exhibits multifunctional capabilities like demultiplexing, filtering, and lasing in a short length of the grating depending on the different operating regimes.

DOI: 10.1103/PhysRevA.102.013515

I. INTRODUCTION

From the invention of mirrors and lenses, and to optical fibers of today, the quest to alter light propagation in a medium seems to be an unceasing one. At present, the field of refractive index engineering has witnessed one of its major milestones in the form of introducing non-Hermitian notions into the traditional optical structures [1–7]. Before familiarization of parity-time-symmetric ($\mathcal{PT}$-symmetric) concepts, overcoming the inherent loss remained as one of the challenging aspects in designing any physically realizable optical structure [8,9]. When most researchers were investigating methodologies to nullify the intrinsic loss, non-Hermitian physicists and mathematicians opted for the manipulation of the inherent loss of the system with the aid of newly designed artifacts known as $\mathcal{PT}$-symmetric structures [2,3,10]. It was figured out that, by judiciously controlling the inherent loss and extrinsic gain, it is possible to realize $\mathcal{PT}$-symmetric systems that can breed many surprising optical phenomena [4,9,11]. Mathematically, the $\mathcal{PT}$-symmetric condition, which is required to breed such optical behavior, is defined in terms of the refractive index as $n(z) = n^*(-z)$. Physically, this kind of complex refractive index profile is achieved in any $\mathcal{PT}$-symmetric structure by means of devising regions of gain and loss built in a counterbalanced architecture [12–14]. Apart from fundamental aspects, research in the field of $\mathcal{PT}$-symmetric optics has strongly changed towards the possibility of employing them in a wide range of applications in next-generation light wave communication systems with larger tunability and reconfiguration [15].

Fiber Bragg gratings (FBGs) are indispensable optical elements extensively employed across diverse fields of physics ranging from simple filters [16–21] to optical signal processing [22,23]. Hill *et al.* discovered that the fiber is vulnerable to intense UV radiation which results in an irreversible alteration of the core index, and thus constituting a periodic index variation in the core [19,24]. Such a repeated periodic pattern composed of small sections of constant period Λ and fixed index n is termed a "grating" [18,25]. It is known that, due to the mismatch between the core and grating indexes, a fraction of the optical signal is reflected at each period [19]. These reflected signals get added up constructively at one selective wavelength known as the Bragg wavelength λ_b. FBGs are extremely wavelength-discriminative devices which strongly reflect back the wavelengths satisfying the Bragg condition (where the photonic band gap gets formed) while the rest of the optical signals are transmitted [20]. Such a wavelength-selective reflection (transmission) phenomenon arises as a consequence of energy coupling between different counterpropagating modes of the FBG.

*vickyneeshraja@gmail.com
†govin.nld@gmail.com
‡drmaha@annauniv.edu
§lakshman.cnld@gmail.com

The wavelength bands which are strongly reflected near the Bragg wavelength are designated as the stopband of the grating. The possibility to easily detune the stopband of the grating stands out to be one of the distinct features of these distributed feedback structures [26,27]. Without a doubt, this must be regarded as the dominant reason which promoted FBG to emerge as a separate research domain today. In addition, it also offers numerous other intriguing features like compactness, inexpensiveness, low insertion, high return loss, and so forth [17–20]. The research field of fiber Bragg gratings can be broadly categorized into two separate regimes, namely, linear and nonlinear domains. The nonlinear domain, which includes the study of gap soliton formation, steering dynamics of the grating structures via optical bistability, and multistability is a fascinating one in the perspective of conventional [21,28–30] and $\mathcal{PT}$-symmetric structures [31,32]. Nevertheless, we confine our investigation here to the study of linear dynamics of phase-shifted periodic structures alone by introducing gain and loss with the reason that the linear system itself is less understood so far from the perspective of $\mathcal{PT}$ symmetry.

Ever since the pioneering work of Agrawal and Radic [16], the phase-shifted FBGs paved the way for the scientific community to unearth many intriguing optical behaviors from the perspective of both linear and nonlinear gratings [16,22,33–36]. With the introduction of a phase shift into the structure, a narrow range of wavelengths inside the stopband of the FBG transmits the incoming optical field. This span of wavelengths can be altered by fine tuning the amount of phase shift [16]. Driven by these luxuries, these phase-shifted FBGs are used to build all-optical demultiplexers [16], low-power all-optical switches [22,33], and signal processing devices [34].

Initially, Kulishov *et al.* [37] formulated the coupled-mode theory of a Bragg grating with gain and loss in the linear regime and also demonstrated the direction-dependent transmission, reflection, delay, and dispersion characteristics of the same system. They further made evident that, if the light-launching condition is reversed, significant amplification of spectra occurs under grating index modulation (real and imaginary) mismatch conditions. Another significant contribution in that work includes the demonstration of reflectionless transmission when the real and imaginary parts of the modulation index are equal. Some of the notable contributions in the field of distributed feedback structures (DFBs) with gain and loss were given by Longhi, which include the demonstration of spectral singularities [38], simultaneous coherent lasing, and absorption behavior [39]. Subsequently, Lin *et al.* demonstrated light propagation dynamics in the context of linear $\mathcal{PT}$-symmetric fiber Bragg grating (PTFBG) at the exact $\mathcal{PT}$-symmetric phase and coined the reflectionless optical wave transmission mechanism as *unidirectional invisibility* [4]. Later, Huang *et al.* extended this concept of $\mathcal{PT}$-symmetry to nonuniform chirped gratings in concatenation with active and passive grating structures [40]. It is worthwhile to recall that the remarkable design of a frequency comb in a supersymmetric (SUSY) DFB structure was exhibited by Longhi [41]. Lupu *et al.* demonstrated the concept of $\mathcal{PT}$ symmetry in an apodized grating with the aid of duty cycle methods [42]. Quite recently, Correa *et al.* came up with the possibility of designing Bragg gratings whose optical dynamics can be described by a Dirac-like equation in the presence of a $\mathcal{PT}$-symmetric Hamiltonian [43]. Following these works, we recently demonstrated that it is possible to construct direction-dependent delay lines and dispersion compensator in a chirped and apodized PTFBG [32]. Furthermore, we would like to construct $\mathcal{PT}$-symmetric FBG structures which can provide narrow-band tunable lasing spectra in terms of intensity, linewidth, and wavelength. Consequently, it is favorable to control the spectra by simply fine tuning the amount of phase shift in the middle section of the grating. This gives the overall motivation and the necessity to investigate the spectral features of phase-shifted $\mathcal{PT}$-symmetric fiber Bragg gratings (PPTFBGs).

Before we investigate the spectral characteristics of our proposed model, we would like to clearly point out the advantages of the system compared with the other configurations reported in the literature to realize a tunable all-optical narrow-band lasing spectra [44–48]. In the context of the aforementioned conventional systems, the insertions of discrete components in the form of Fabry-Pérot filters and saturable absorbers to achieve narrow-band wavelength selectivity (bandpass) into the system contribute to insertion loss [45,47]. The amplification at the sidelobes of the spectra need to be eliminated by employing an apodized FBG. However, it unnecessarily truncates the spectral response in the absence of chirping [49–51]. These configurations demand the use of an extra-gain fiber (Er^{3+}) having a larger length in the ring for stabilization which increases the overall length of the system to the order of meters [44,45]. It is important to remember that the higher the number of discrete components in a system, the higher will be the loss, which reduces the compactness and reconfigurability of the system. But a broken phase-shifted $\mathcal{PT}$-symmetric FBG model, illustrated in this work, has an edge over the conventional systems to realize a narrow-band lasing spectra, as illustrated in the following sections. The same phase-shifted PTFBG itself will do the filtering, amplification, and side-lobe suppression without a need for additional discrete components. Moreover, the length of the phase-shifted PTFBG proposed in this work is of the order of millimeters. This has a definite role in increasing the compactness of the overall system. Moreover, the same device can be configured to function as a demultiplexer and phase-shifted modulator in the unbroken $\mathcal{PT}$-symmetric regime.

To accomplish our above motivation, we segment the remaining part of this article as follows: Section II illustrates the mathematical model of the proposed system. In Sec. III A, we investigate the grating characteristics of the proposed system in the unbroken $\mathcal{PT}$-symmetric regime followed by the demonstration of unidirectional wave transport phenomenon at the exceptional point in Sec. III B. The lasing behavior in the broken $\mathcal{PT}$-symmetric regime is elucidated in Sec. III C. Finally, the article is concluded in Sec. V.

II. MATHEMATICAL MODEL

We consider a $\mathcal{PT}$-symmetric refractive index distribution $n(z)$ that includes the effect of a discrete phase shift ϕ, which is introduced in the middle of the periodic structure ($z = 0$). The total distance L is divided into many small unit cells with

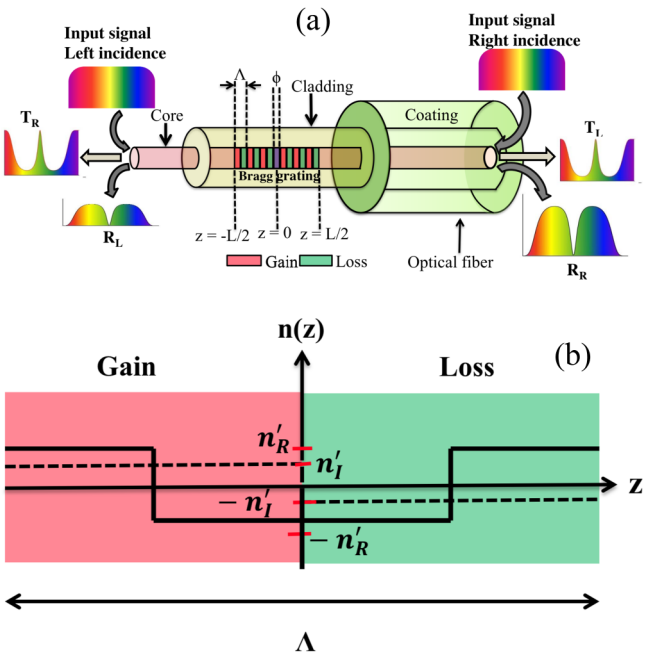

FIG. 1. (a) Schematic of a phase-shifted $\mathcal{PT}$-symmetric fiber Bragg grating (PPTFBG) where two uniform PPTFBGs each having a length of $L/2$ and separated by a phase shift ϕ in the middle of the structures. (b) Each unit cell of the uniform structure with grating period Λ consists of equal gain regions (green) and loss regions (red) to maintain the $\mathcal{PT}$-symmetric refractive index $n(z)$.

each having a grating period Λ (see Fig. 1). The refractive index distribution is given by

$$n(z) = n_0 + n_{1R}\cos\left(\frac{2\pi}{\Lambda}z + \phi\right) + in_{1I}\sin\left(\frac{2\pi}{\Lambda}z + \phi\right), \tag{1}$$

where n_0, n_{1R}, and n_{1I} represent the effective refractive index of the core and the real and imaginary parts of the grating's modulation strength, respectively. It is to be noted that Eq. (1) refers to the gradually varying sinusoidal profile that may be hard to fabricate in a real situation. To overcome this, one can employ square wave forms instead of sinusoidal forms, as shown in Fig. 1(b). This will enable one to study the entire structure consisting of each unit cell of length l obeying sine and cosine modulations of the considered profile in Eq. (1). Also, it is assumed that the real (n_{1R}) and imaginary (n_{1I}) parts of the modulation strength are weak perturbations when compared with the uniform index of the background material (n_0), *viz.*, n_{1R}, $n_{1I} \ll n_0$ [4]. Hence, after neglecting the higher-order terms, the equation resulting from squaring Eq. (1) can be reduced to the final form,

$$n^2(z) = n_0^2 + 2n_0n_{1R}\cos(2\pi/\Lambda z + \phi) + 2n_0n_{1I}\sin(2\pi/\Lambda z + \phi). \tag{2}$$

Equation (2) can be rewritten as

$$n^2(z) = n_0^2 + n_0(n_{1R} + n_{1I})\exp\left(\frac{2i\pi}{\Lambda}z + \phi\right) + n_0(n_{1R} - n_{1I})\exp\left(\frac{-2i\pi}{\Lambda}z + \phi\right). \tag{3}$$

The coupled-mode equations that describe the system of interest can be found by substituting the refractive index distribution given in Eq. (1) into the time-independent Helmholtz equation. It describes the propagation characteristics of the incoming optical field inside the $\mathcal{PT}$-symmetric optical structure [4], which can be given by

$$\frac{d^2E}{dz^2} + k^2\left(\frac{n^2(z)}{n_0^2}\right)E = 0. \tag{4}$$

In Eq. (4), k stands for the wave vector and E describes the optical field as a superposition of forward and backward fields traveling inside the grating, and it reads

$$E = E_f(z)\exp(ikz) + E_b(z)\exp(-ikz), \tag{5}$$

where E_f and E_b refer to the slowly varying amplitudes of forward and backward propagating fields, respectively. Note that, based on the slowly varying envelope approximation, the second derivatives of the forward (E_f'') and backward field (E_b'') envelopes can be neglected. On substituting Eqs. (5) and (3) together in Eq. (4) and averaging over the rapidly oscillating terms $\exp[\pm i(\frac{2\pi}{\Lambda}z + \phi + kz)]$ by synchronous approximation, the resulting equation reads

$$\begin{aligned} 0 = {} & 2ikE_f'\exp(ikz) - 2ikE_b'\exp(-ikz) \\ & + k^2\frac{(n_{1R} + n_{1I})}{n_0}E_b\exp\left[i\left(\frac{2\pi}{\Lambda}z + \phi - kz\right)\right] \\ & + k^2\frac{(n_{1R} - n_{1I})}{n_0}E_f\exp\left[-i\left(\frac{2\pi}{\Lambda}z + \phi - kz\right)\right]. \end{aligned} \tag{6}$$

We can check that Eq. (6) implies the following system of first-order coupled linear differential equations for the forward- and backward-propagating fields E_f and E_b, respectively:

$$\begin{aligned} 0 = {} & k\frac{(n_{1R} + n_{1I})}{n_0}E_b\exp\left[i\left(\frac{2\pi}{\Lambda}z + \phi - kz\right)\right] \\ & + 2iE_f'\exp(ikz), \end{aligned} \tag{7}$$

$$\begin{aligned} 0 = {} & k\frac{(n_{1R} - n_{1I})}{n_0}E_f\exp\left[-i\left(\frac{2\pi}{\Lambda}z + \phi - kz\right)\right] \\ & - 2iE_b'\exp(-ikz). \end{aligned} \tag{8}$$

From the fundamental definition of wave vector, the standard forms of coupling (κ) and gain-loss coefficients (g) read [4,31,32,52,53]

$$kn_{1R}/2n_0 = \pi n_{1R}/\lambda = \kappa, \quad kn_{1I}/2n_0 = \pi n_{1I}/\lambda = g, \tag{9}$$

where λ is the operating wavelength. Also, the detuning parameter is given by

$$\delta = 2\pi n_0\left(\frac{1}{\lambda} - \frac{1}{\lambda_b}\right), \tag{10}$$

where $\lambda_b = 2n_0\Lambda$. Substituting these standard notations into Eqs. (7) and (8), Eqs. (7) and (8) can be rewritten as

$$\frac{dE_f}{dz} = i(\kappa + g)e^{i\phi}e^{-2i\delta z}E_b, \tag{11}$$

$$\frac{dE_b}{dz} = -i(\kappa - g)e^{-i\phi}e^{2i\delta z}E_f. \tag{12}$$

The resulting coupled-mode equations that describe the proposed system can be found out by substituting transformations, $u,\ v = E_{f,b}\exp(\mp i\delta z)$ [32] in Eqs. (11) and (12), which read [22,32]

$$0 = +i\frac{du}{dz} + \delta u + (\kappa + g)e^{i\phi}v, \tag{13}$$

$$0 = -i\frac{dv}{dz} + \delta v + (\kappa - g)e^{-i\phi}u, \tag{14}$$

where u, v, z, δ, κ, and g correspond to forward and backward field amplitudes, the spatial coordinate, detuning, coupling, and gain-loss parameter, respectively.

Since the central theme of the article is to demonstrate tunable spectral characteristics of a PPTFBG by varying the magnitude of the phase-shift (PS) in the middle of the grating, it is important to comment on the existing techniques for the fabrication of phase-shifted fiber Bragg gratings (PFBGs). This includes the UV postprocessing [54], moving fiber-scanning beam method [55], CO_2 laser irradiation [56], shielded phase mask method [57], Moiré method [58], and so on. A detailed comparative study of various fabrication techniques to realize a PFBG was outlined by Chehura *et al.*, and they concluded that the scanning beam method is comparatively advantageous over other existing methods [59]. Even though this technique is simple and more reliable, the magnitude of PS etched on the structure cannot be varied, once it is fabricated. For some specific applications (as enumerated previously), the magnitude of the PS needs to be tunable rather than remaining static. Under such circumstances, one should opt for a fabrication process that would allow dynamical variation in the PS value, post the formulation of the device. Some of the widely used techniques in this context includes the in-grating bubble technique [60], mechanical tuning with piezoelectric transducers [61], and the heating element method [62]. Each one of the aforementioned techniques possess some disadvantages and the cost ineffectiveness is one of the major concerns among all. Falah *et al.* came up with an idea of a *four-point beam bending arrangement*, which would allow for tuning the PS value via variation in the optical path by spatially varying the strain within the periodic structure through the micrometer screw adjustment [63]. This method was proven to possess set-and-forget capability, consume less power, and be tunable over the full scale range of PS from 0 to 2π. More importantly, the degree of accuracy of the PS value achieved with respect to the micrometer screw variation was found to show good agreement with theoretical results. Recently, a variable-velocity scanning method was proposed by Zhou *et al.* which allows fabrication of PFBGs with asymmetric uniform grating section on either side of the PS region [64]. Even though it is experimentally established that it is possible to obtain tunable PFBGs, we confine our investigation to the symmetric PFBGs (consisting of two uniform grating structures with each a length of $L/2$ with PS placed in their middle) with equal gain and loss as shown in Fig. 1. With this brief note, we affirm that our proposed model is experimentally realizable, and applications such as tunable lasing can be established with ease, thanks to the ability of the structure to provide a tunable phase shift.

Although the mathematical model (13) and (14) of the system can be solved by the direct-integration technique with standard FBG boundary condition, the phase-shifted FBG with gain and loss shown in Fig. 1 can also be investigated with the aid of the transfer-matrix method (TMM) (piecewise uniform technique) [16,32]. This is a most commonly used technique to model a linear and nonuniform FBG, and it also gives a clear picture of the practical realization of these structures. Moreover, the investigation of the spectra of the grating becomes a relatively simple task because this method is faster than the direct-integration approach in the case of more complicated grating physical structures. The modeling of a phase-shifted FBG system relies on the fact that the overall structure is formed by concatenating two uniform and symmetric FBGs with a phase-shift value of ϕ in between them [17]. The phase shift ϕ at $z = 0$ can be inserted by simply multiplying the matrix corresponding to the first uniform FBG (M_1) with the diagonal matrix (M_{ph}) having elements $\exp(\pm i\phi/2)$ followed by a second uniform FBG (M_2). Thus, the resultant second-order matrix F that describes the overall system reads

$$F = M_1 \times M_{ph} \times M_2. \tag{15}$$

Hence, the input and output fields are related by

$$\begin{bmatrix} u_n \\ v_n \end{bmatrix} = M_1 \times M_{ph} \times M_2 \begin{bmatrix} u_0 \\ v_0 \end{bmatrix}. \tag{16}$$

Here u_n, v_n represent the output amplitudes as a function of input amplitudes u_0, v_0 and M_1, M_2 denote the matrices which relate the input and output fields of two uniform FBGs separated by the discrete phase-shift ϕ. Modeling the uniform $\mathcal{PT}$-symmetric grating ($-L/2 \leqslant z < 0$ and $0 < z \leqslant L/2$) requires dividing the length of the uniform grating ($\hat{L} = L/2$) into n number of small sections of each of length l [32]. Each piecewise section of length l is modeled by a corresponding matrix $m_1, m_2, \ldots, m_n$ and hence the uniform gratings of length $\hat{L}$ are represented by the product matrices

$$M_1 = M_2 = m_1 m_2 m_3 \cdots m_{n-1} m_n, \tag{17}$$

$$m_1 = \begin{bmatrix} m_{11} & m_{12} \\ m_{21} & m_{22} \end{bmatrix}, \tag{18}$$

where

$$\begin{aligned} m_{11} = m_{22}^* &= \cosh(\hat{\sigma} l) + i\left(\frac{\delta}{\hat{\sigma}}\right)\sinh(\hat{\sigma} l), \\ m_{12} &= i\left(\frac{\kappa + g}{\hat{\sigma}}\right)\sinh(\hat{\sigma} l), \\ m_{21} &= -i\left(\frac{\kappa - g}{\hat{\sigma}}\right)\sinh(\hat{\sigma} l). \end{aligned} \tag{19}$$

The procedure in which the TMM elements in Eq. (19) are calculated is straightforward. By considering the harmonic solutions in the form of $u, v = A_f, A_b \exp(i\hat{\sigma} z)$, one arrives at the dispersion relation for the common propagation constant for $m_1, m_2, \ldots, m_n$ as, $\hat{\sigma} = (\kappa^2 - g^2 - \delta^2)^{1/2}$. Once the propagation constant is found, the appropriate boundary values are applied to the Bragg gratings to arrive at the matrix elements.

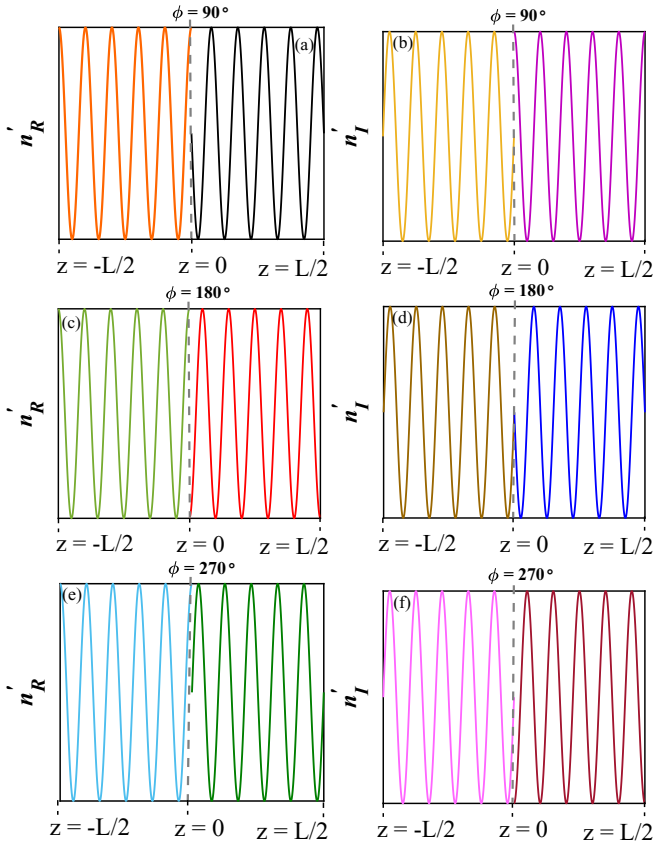

FIG. 2. Schematics of the variation of real and imaginary parts of refractive index for various phase-shift values are drawn in the left and right panels, respectively. They are plotted at a phase of (a), (b) $\phi = 90^\circ$, (c), (d) $\phi = 180^\circ$, (e), (f) $\phi = 270^\circ$. In all the plots, one can observe that the different phase values contribute to the various types of refractive index profiles which predominantly get changed in the middle of the device with respect to the phase values ranging from 90° to 270°.

Also, the matrix that represents the phase-shift region is given by [17]

$$M_{ph} = \begin{bmatrix} \exp(i\phi/2) & 0 \\ 0 & \exp(-i\phi/2) \end{bmatrix}. \tag{20}$$

Note that the phase shift ϕ is introduced in the middle of the grating such that, on either side of the phase-shift region, we have two uniform FBGs, as indicated in Fig. 1(a). Each uniform PTFBG features a number of alternating regions of gain and loss. A single unit cell of period Λ is constituted by having a real $[n_R' = n_{1R}\cos(2\pi z/\Lambda + \phi)]$ and imaginary $[n_I' = i\, n_{1I}\cos(2\pi z/\Lambda + \phi)]$ modulation of the refractive index, as shown in Fig. 4(b). Figures 2(a)–2(f) show the corresponding variation in n_R' and n_I' when a particular value of phase shift is included into the system. To elucidate further, when $z < 0$, the modulations of refractive index profile are unperturbed by the phase shift ($\phi = 0$). At $z = 0$, the phase term ϕ is added to the modulation profile in the middle of the grating and thus we visualize discontinuities (exactly in the middle) in the n_R' and n_I' profiles. For $z > 0$, these profiles get changed with the modified phase and thus the two uniform PTFBGs feature a difference in the phases of ϕ. These variations in n_R' and n_I' are responsible for the presence of a narrow transmission band within the stopband of the grating, as indicated in Fig. 4(a). The location of this transmission band is dictated by the amount of phase shift ϕ in the middle.

The resultant matrix F reads

$$F = \begin{bmatrix} F_{11} & F_{12} \\ F_{21} & F_{22} \end{bmatrix}, \tag{21}$$

where

$$\begin{aligned} F_{11} &= M_{11}^2 e^{i\phi/2} + M_{12}M_{21}e^{-i\phi/2}, \\ F_{12} &= M_{11}M_{12}e^{i\phi/2} + M_{12}M_{22}e^{-i\phi/2}, \\ F_{21} &= M_{21}M_{11}e^{i\phi/2} + M_{22}M_{21}e^{-i\phi/2}, \\ F_{22} &= M_{12}M_{21}e^{i\phi/2} + M_{22}^2 e^{-i\phi/2}. \end{aligned} \tag{22}$$

Thus the reflected and the transmission amplitudes of full PPTFBGs can be found from the final matrix F as

$$r_L = -F_{21}/F_{22} = -\frac{M_{11}M_{21}\exp(i\phi) + M_{21}M_{22}}{M_{12}M_{21}\exp(i\phi) + M_{22}^2}, \tag{23}$$

$$r_R = F_{12}/F_{22} = \frac{M_{11}M_{12}\exp(i\phi) + M_{12}M_{22}}{M_{12}M_{21}\exp(i\phi) + M_{22}^2}, \tag{24}$$

$$t_L = t_R = t = |F_{11}F_{22} - F_{12}F_{21}|/F_{22} = 1/F_{22}. \tag{25}$$

After some mathematical manipulations, using Eq. (19), the explicit relation for the reflection and transmission amplitudes can be found as

$$r_L = \frac{i(\kappa - g)\left[\hat{\sigma}\, r_1(1 + e^{i\phi}) - i\delta r_1^2(1 - e^{i\phi})\right]}{\kappa^2 - g^2\left(1 + r_1^2 e^{i\phi}\right) - \delta^2\left(1 + r_1^2\right) - 2i\delta\hat{\sigma}\, r_1}, \tag{26}$$

$$r_R = \frac{i(\kappa + g)\left[\hat{\sigma}\, r_1(1 + e^{i\phi}) - i\delta r_1^2(1 - e^{i\phi})\right]}{\kappa^2 - g^2\left(1 + r_1^2 e^{i\phi}\right) - \delta^2\left(1 + r_1^2\right) - 2i\delta\hat{\sigma}\, r_1}, \tag{27}$$

$$t = \frac{e^{i\phi/2}\hat{\sigma}^2\,\mathrm{sech}^2(\hat{\sigma} z)}{\kappa^2 - g^2\left(1 + r_1^2 e^{i\phi}\right) - \delta^2\left(1 + r_1^2\right) - 2i\delta\hat{\sigma}\, r_1}. \tag{28}$$

In Eqs. (26)–(28), $r_1 = \tanh(\hat{\sigma} L)$.

Furthermore, if the applications pertaining to optical network communications demand more than a few transmission windows within the stop band of the spectra, one can make use of the concept of introducing multiple phase shifts, as discussed below [16].

The multiple phase-shift regions can be modeled mathematically by including the phase matrix at the respective locations in the combined transfer matrix. As an example shown in Fig. 3, the first, second, and third phase-shift regions z_1, z_2, z_3 are located at $z = -L/4$, 0, and $L/4$, respectively, and the corresponding phase matrices are given by M_{ph1}, M_{ph2}, and M_{ph3}. Then we can identify a matrix M_1 which represents the matrix that accounts for the resultant of all the small grating sections from $z = -L/2$ to $z = -L/4$. Similarly, M_2 represents the combined matrix obtained by cascading all the individual grating sections from $z = -L/4$ to $z = 0$. Likewise, M_3, M_4 represent the matrix acquired by cascading the individual grating sections between $z = 0$ to $z = L/4$ and $z = L/4$ to $z = L/2$, respectively. The resultant matrix M which stands for the overall structure from $z = -L/2$ to $z = L/2$ is

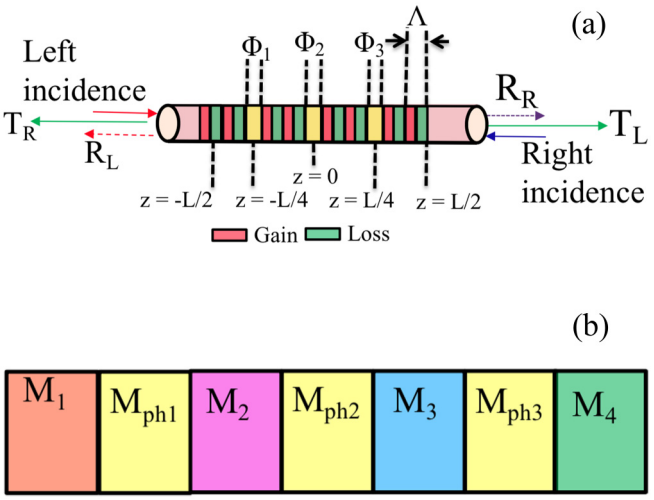

FIG. 3. (a) Schematic of multiple phase-shifted PTFBGs with phase-shift regions located at $z = -L/4$, 0, $L/4$. (b) Portrays the implementation of the transfer-matrix method for the multi-phase-shift scheme.

given by

$$M_{\text{multi}} = M_1 \times M_{ph1} \times M_2 \times M_{ph2} \times M_3 \times M_{ph3} \times M_4. \tag{29}$$

It is to be noted that the explicit mathematical form in the case of multiple phase shift is cumbersome to find and hence the reflection and transmission amplitudes are computed from the transfer-matrix routine and are given by

$$r_L = -M_{21_{\text{multi}}}/M_{22_{\text{multi}}}, \quad r_R = M_{12_{\text{multi}}}/M_{22_{\text{multi}}},$$
$$t = \det(M_{\text{multi}})/M_{22_{\text{multi}}}. \tag{30}$$

Finally, the reflection and transmission coefficients can be expressed as

$$R_L = |r_L|^2, \quad R_R = |r_R|^2, \quad T = |t|^2. \tag{31}$$

Throughout this paper, the length L and the coupling coefficient κ of the device are taken to be 4 mm and 10 cm^{-1}, respectively (unless specified).

III. SPECTRAL CHARACTERISTICS OF PPTFBG WITH A SINGLE PHASE-SHIFTED REGION

A. Unbroken $\mathcal{PT}$-symmetric regime

In this section, the value of the gain and loss parameter is varied in the range $0 < g < 10$ cm^{-1} to maintain the unbroken $\mathcal{PT}$-symmetric condition $\kappa > g$. We also recall that a phase-shifted FBG behaves like a transmission filter with a very narrow bandwidth. In this section, we consider such a phase-shifted $\mathcal{PT}$-symmetric FBG with a truncated spectral response between 1549.6 to 1550.4 nm and thus the plots are scaled between these wavelengths, as shown in Figs. 4 and 5.

The magnitude and phase response of an unbroken $\mathcal{PT}$-symmetric FBG ($g = 8$ cm^{-1}) is very much similar to a conventional phase-shifted FBG ($g = 0$) except that it is possible to alter the transmittivity and reflectivity by tuning the value of gain-loss. In the absence of phase shift ($\phi = 0$), the device is predominantly reflective rather than transparent for the wavelengths between 1549.7 and 1550.3 nm, as indicated by the dotted lines in Figs. 4(c) and 4(e). But with the introduction of phase shift in the middle, a narrow band of wavelengths within the stop band transmits the incoming light, as indicated by the dashed ($\phi = 90°$), solid ($\phi = 180°$), and dash-dotted lines ($\phi = 270°$) in Fig. 4(a). At one particular wavelength λ_2 [see inset of Fig. 4(g), which is same for T and R_R also], the transmittivity reaches its maximum (unity) inside the stopband of the grating. At this wavelength, we can observe a peak in the transmission spectra, as seen in Fig. 4(a), and a dip in the corresponding reflection spectra, as shown in Figs. 4(c) and 4(e). The response of the grating is asymmetric for all the values of phase except for $\phi = 180°$ as referred from

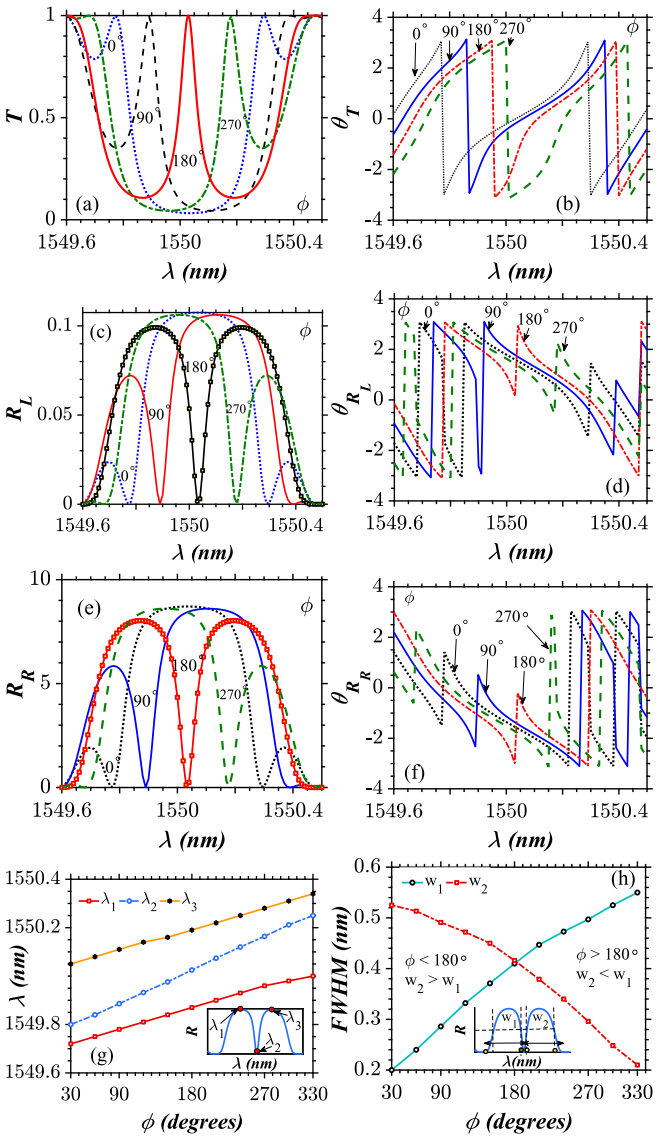

FIG. 4. (a)–(f) Illustrates the reflection and transmission spectra of an unbroken PPTFBG for different values of phase shift $\phi = 0°$, 90°, 180°, and 270°, respectively. The intensity plots are given in the left panel whereas the right panels correspond to phase plots. (g) Shows the variation in λ_1, λ_2, and λ_3 with increase in phase ϕ for R_L. The variations in the full width half maximum (FWHM) of the spectra on either sides of λ_2 (w_1 and w_2) with respect to change in phase ϕ is shown in panel (h).

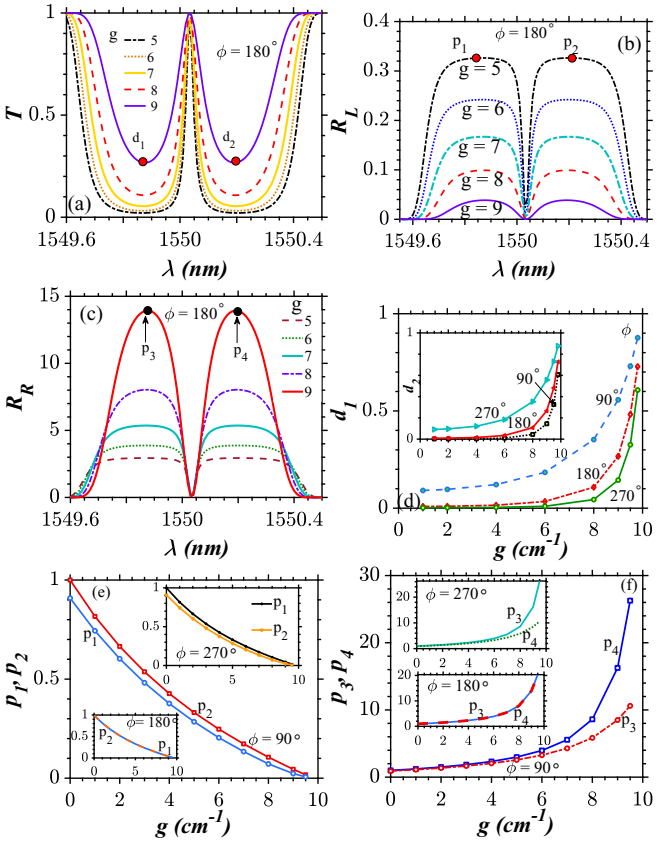

FIG. 5. The variation in the transmission and reflection characteristics of a unbroken PPTFBG with respect to variation in the gain and loss parameter g is plotted in panels (a)–(c). The continuous variation of minimum of transmitted intensity (d_1 and d_2) against the parameter g is plotted in panel (d). Panels (e) and (f) show the continuous variation of maximum of reflected intensities (p_1, p_2, p_3, and p_4) against variation in gain-loss parameter g.

these plots. For $\phi = 180^\circ$, the narrow transmission window occurs exactly in the middle of the spectra and on either side of the transmission peak, the spectrum is symmetrical. The wavelength λ_2 at which maximum transmission within the stopband occurs is shifted towards longer wavelengths by increasing the phase. Moreover, the wavelengths λ_1, λ_3 at which peak reflection occurs on either side of λ_2 are also shifted towards higher wavelengths, as shown in Fig. 4(g). The magnitude plots obtained for a phase of $\phi = 270^\circ$ is exactly the mirror image of the spectra obtained for a phase of $\phi = 90^\circ$, as shown in Figs. 4(a), 4(c), and 4(e).

To illustrate the spectral response further, we define another useful parameter, namely, the *full width at half maximum* (FWHM). It indicates the difference between the two wavelengths corresponding to $R = 1/2\ R_{\max}$. For $\phi < 180^\circ$, the FWHM of the reflection spectra on the longer-wavelength (w_2) side of λ_2 is broader than the one (w_1) on the shorter-wavelength side of λ_2, as shown in Fig. 4(h). At, $\phi = 180^\circ$, these FWHMs are equal ($w_1 = w_2$). On the other hand, when $\phi > 180^\circ$, the FWHM of the spectra on the right side of λ_2 (w_2) is narrow compared with the one on the left (w_1) of λ_2. A well-known application of phase-shifted FBG is that it can be used as channel selector (demultiplexer). To implement

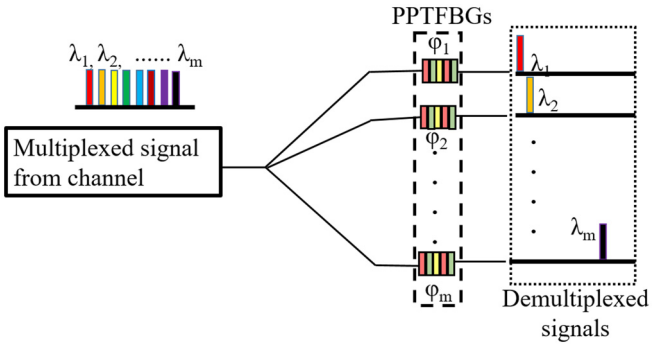

FIG. 6. Schematic of all-optical demultiplexer with m-array of PPTFBGs having different phase-shift values (ϕ_1, ϕ_2, …, ϕ_m) for selecting m individual wavelengths (λ_1, λ_2, ...λ_m) from a multiplexed input.

such a scheme, a multiplexed signal emerging from a transport fiber is then passed into the array of FBGs (m-FBGs for m-channels) with each FBG having a particular phase shift ϕ for selecting a particular channel. This is facilitated by the inherent property of phase-shifted FBGs to allow a shift in λ_2 and the wavelength of the peaks (λ_1 and λ_3) on either side of λ_2. An unbroken PPTFBG provides an additional degree of freedom to tune the intensity of these peaks, as illustrated in Fig. 5. From Figs. 4(b), 4(d), and 4(f), we find that the phase (θ_T, θ_{R_L}, and θ_{R_R}) responses of the system rely on the gain-loss parameter g and the magnitude of the phase shift ϕ in the middle. Physically, this would mean that the phase of the reflected and transmitted signals is strongly influenced by the changes in the energy of the wave packet as a consequence of variation in gain-loss potential [4] and the value of phase shift.

Like any other $\mathcal{PT}$-symmetric FBG configuration, our system also demonstrates an increase (decrease) in the reflectivity for right (left) light incidence with an increase in the value of the gain-loss parameter g, as illustrated in Figs. 5(e) and 5(f). For $\phi < 90^\circ$, the magnitude of the reflection spectra on the longer-wavelength side of λ_2 is larger than the peak of reflection on the shorter-wavelength side and this is true for both left ($p_2 > p_1$) and right ($p_4 > p_3$) light incidences. When $\phi = 180^\circ$, the magnitudes of these peaks are equal ($p_1 = p_2$ and $p_3 = p_4$). However, when $\phi > 180^\circ$, the opposite effect occurs ($p_1 > p_2$ and $p_3 > p_4$). The increase in the value of gain-loss also contributes to the increase in the magnitude of the dip (d_1 and d_2) with an increase in gain-loss in the transmission spectra, as portrayed in Fig. 5(d). Thus, it is possible to construct all-optical demultiplexers with tunable intensity and spectral width with the proposed $\mathcal{PT}$-symmetric system as shown in Fig. 6.

B. Unidirectional wave transport at the exceptional point

Mathematically, if a $\mathcal{PT}$-symmetric device satisfies the condition $\kappa = g$, then it is known to be working at the exceptional point. It is reported in the literature that different $\mathcal{PT}$-symmetric FBGs, namely uniform [4], apodized [42], and chirped and apodized FBGs [32] exhibit unidirectional wave transport at the exact $\mathcal{PT}$-symmetric phase. From the numerical study presented here, we also confirm that this phenomenon persists even in the presence of phase shift in

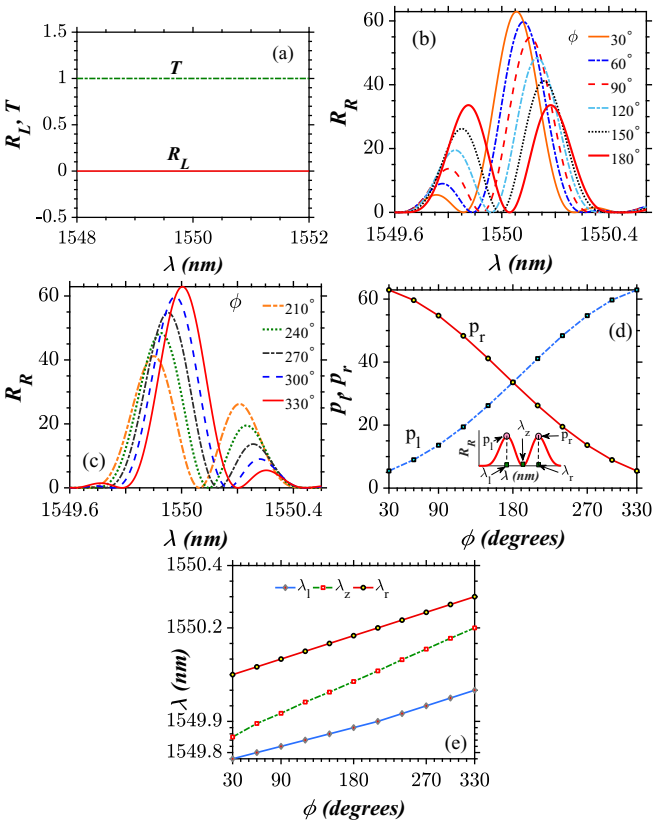

FIG. 7. (a) Phase-independent unidirectional wave transport in a PPTFBG. (b), (c) Phase dependent reflection spectra for the right light incidence at the exceptional point of a PPTFBG. The continuous variation of the reflection peaks (p_l and p_r) against variation in phase ϕ is plotted in panel (d). The wavelengths λ_l, λ_r corresponding to the peaks p_l, p_r in panel (d) and the dip wavelength λ_z are plotted in panel (e).

the middle of the grating. The incident light travels inside the device and emanates at the other end of the grating for the left light incidence as if there is no grating present in the propagating path to reflect the signal ($T = 1$ and $R = 0$), as shown in Fig. 7(a). However, the right incident light shows changes with respect to variations in the value of phase shift ϕ, as depicted in the remaining plots from Figs. 7(b)–7(e). The wavelength corresponding to zero reflectivity within the stop band at the exceptional point is designated as λ_z. On either side of this wavelength, the reflected spectra exhibit peaks (p_l and p_r) which are very similar to the dynamics obtained in the unbroken $\mathcal{PT}$-symmetric regime, except that the magnitude of these peaks are larger because the system operates at a higher value of gain-loss ($g = 10$ cm^{-1}). For example, $R_{R_{\max}}$ measures a magnitude of 54.72 at the exceptional point, whereas, in the unbroken regime ($g = 9.5$ cm^{-1}), it is measured to be 26.25 for a phase of $\phi = 90°$. Unlike the reflection dynamics for the right light incidence reported in other PTFBGs structures at the exceptional point [4,40,42], these structures are not completely reflective to all wavelengths within the stopband, thanks to the presence of phase shift in the middle of the grating. To illustrate this point, for a phase of $\phi = 180°$ and $\lambda = 1550.04$ nm, R_R is measured to be zero. We designate the wavelength corresponding to the

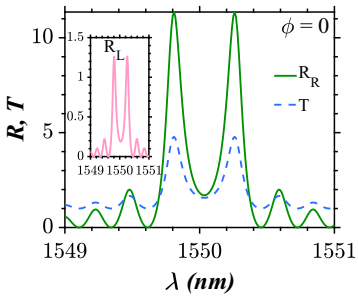

FIG. 8. Spectral characteristics of a broken $\mathcal{PT}$-symmetric FBG in the absence of phase shift ($\phi = 0°$).

zero-reflectivity dip within the stopband as λ_z, at the exact $\mathcal{PT}$-symmetric phase. The wavelengths corresponding to the peaks p_l and p_r are given by λ_l and λ_r. All these wavelengths shift toward longer wavelengths of the spectra with increasing ϕ, as shown in Fig. 7(e).

C. Broken $\mathcal{PT}$-symmetric regime

As well known, a broken $\mathcal{PT}$-symmetric FBG needs to obey the mathematical condition $g > \kappa$ and hence the gain-loss parameter value is kept at $g = 20$ cm^{-1} throughout this section and the tuning is achieved by varying the phase (ϕ). Before investigating the phase-shifted system, it is important to look at the spectral response of the system in the absence of phase shift ($\phi = 0°$). Instead of amplification at the center wavelength, the maximum amplification occurs on both the longer- and shorter-wavelength sides of the Bragg wavelength and the amplification at λ_b is suppressed but not to zero. Also, amplification at the side lobes is visible in Fig. 8.

1. Single-mode lasing behavior

When ϕ is increased to 45°, the reflections in the side lobes which were existing in the absence of phase shift ($\phi = 0°$) are inhibited to a large extent, as shown in Fig. 9(a). But some weak reflections still persist in the spectra corresponding to the right incidence but it is comparably much less than the maximum intensity ($R_{R_{\max}}$). Even these weak reflections are suppressed further when ϕ is increased ($\phi = 60°$) and thus we obtain the pure single-mode lasing behavior shown in Fig. 9(b). The maximum transmittivity (reflectivity) of the single-mode lasing spectra is observed for $\phi = 90°$, as shown in Figs. 9(c) and 9(d). It is important to mention that the side lobes are significantly reduced by tuning the value of phase shift without a need for an apodization technique. Tuning the value of phase also has a drastic effect on the wavelength λ_p corresponding to the peaks of the lasing spectra. From Fig. 9(e), we confirm that λ_p is shifted to the longer wavelengths of the spectra with an increase in ϕ. The reflectivity and transmittivity get increased proportionally to an increase in ϕ, whereas the FWHM shows an inverse relationship with the increase in ϕ, as shown in Fig. 9(f). This means that higher the peak reflectivity $R_{\max}$ and transmittivity $T_{\max}$, the narrower the FWHM of the lasing spectra, and this is indeed the most desired characteristic feature of a typical lasing spectrum.

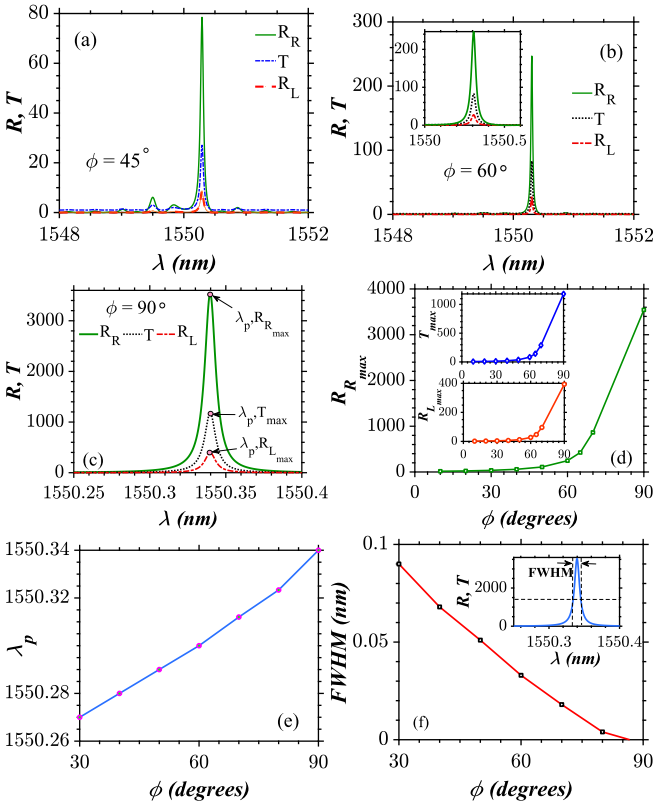

FIG. 9. Phase-controlled single-mode lasing behavior of a broken PTFBG against the variation in phase shift at $g = 20$ for different phases $\phi = 45^\circ$, 60°, and 90° is shown in panels (a)–(c), respectively. The continuous variation of maximum of transmitted ($T_{\max}$) and reflected intensities ($R_{\max}$) with respect to change in ϕ is shown in panel (d) and the wavelengths λ_2 corresponding to the peaks are shown in panel (e). The change in the FWHM of the transmitted and reflected spectra against the variation in ϕ is plotted in panel (f).

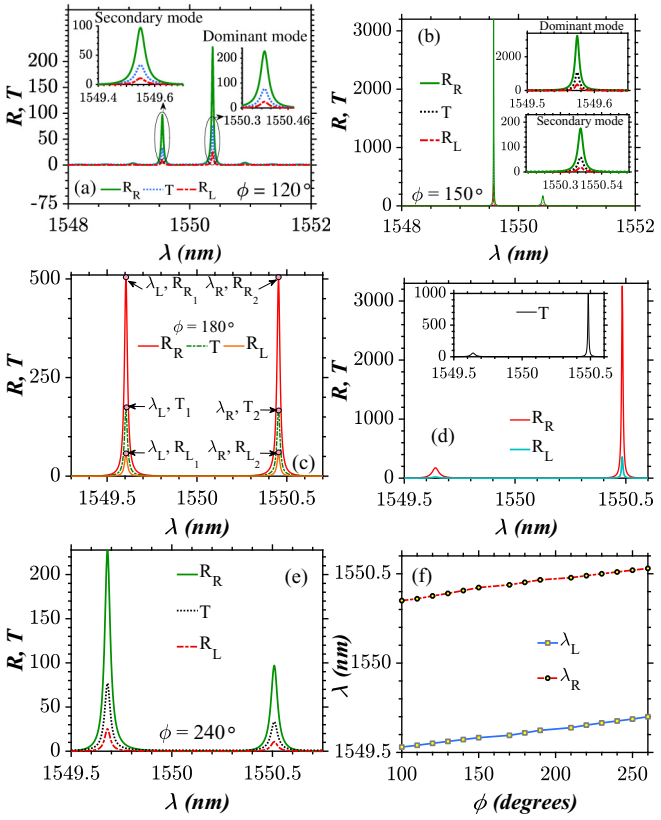

FIG. 10. Dual-mode lasing behavior exhibited by a broken $\mathcal{PT}$-symmetric FBG at $g = 20$ against the variation in phase shift with $\phi = 120^\circ$, 150°, 180°, 210°, 240° is shown in panels (a)–(e), respectively. The variation in the wavelengths corresponding to the reflectivity peaks λ_l and λ_r of the spectra is plotted in panel (f).

2. *Dual-mode lasing behavior*

The peaks of reflectivity and transmittivity in the spectra are found to occur at two wavelengths for values of phase falling in the range $90^\circ < \phi < 270^\circ$. To differentiate them, they are designated here as dominant and secondary modes as shown in Figs. 10(a)–10(c). The former has larger amplification at the peak ($R_{\max}$ and $T_{\max}$) compared with the latter one. The reflectivity and transmittivity at the peaks between these two modes are always asymmetrical except for certain values of ϕ, say $\phi = 180^\circ$. For a phase shift of $\phi = 120^\circ$, the dominant (secondary) mode occurs on the left (right) of the Bragg wavelength (1550 nm), as illustrated in Fig. 10(a). On the other hand, when $\phi = 150^\circ$ the dominant and the secondary modes are seen on the shorter- and longer-wavelength sides of the Bragg wavelength, respectively, as shown in Fig. 10(b). However, both these modes are equally amplified at the phase $\phi = 180^\circ$, as depicted in Fig. 10(c). Post the occurrence of the symmetric amplification at 180°, the asymmetric nature of amplification between these two modes begins to appear. As portrayed in Fig. 11(d), the appearance of dominant and secondary modes at a phase of $\phi = 210^\circ$ looks like the plots obtained for a phase of $\phi = 150^\circ$ in terms of intensity with the center wavelength interchanged. It is confirmed from Fig. 10(e) that the spectrum shown by the system for a phase of $\phi = 240^\circ$ is exactly the mirror image of the plot at $\phi = 120^\circ$ about the Bragg wavelength (1550 nm). Finally, we look into the impact of phase on the wavelength at which peak reflectivity occurs in Fig. 10(f). The reflectivity and transmittivity peaks on the shorter-wavelength side (λ_L) of 1550 nm are shifted towards the Bragg wavelength, whereas the corresponding peaks on the longer-wavelength side (λ_R) of 1550 nm are shifted further away from the Bragg wavelength. From the continuous variation of the intensity plots against the variation in the value of phase ϕ depicted in Figs. 11(a)–11(d), we infer that the PPTFBG system exhibits both increasing and decreasing lasing behavior in both reflection and transmission spectra depending on the phase shift ϕ. As stated in the previous section, the FWHM is narrower for those values of ϕ for which reflectivity and transmittivity of the spectra is larger and vice versa, and this behavior is plotted in Fig. 11(e). For some values of ϕ, the device shows lasing spectra with very huge reflectivity of the order of 10^4 in its light propagation characteristics (R and T) when operated in the broken $\mathcal{PT}$-symmetric regime. Such behavior is plotted in Fig. 12(a) at a phase of $\phi = 160^\circ$. These types of uncontrollable amplification in the lasing spectra are found to decrease upon increasing the length of the grating, as shown in Fig. 12(b).

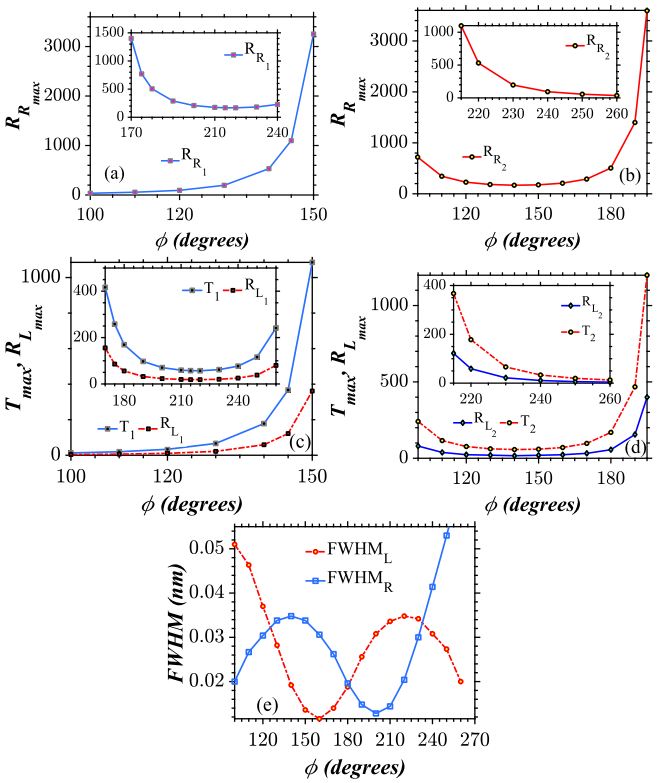

FIG. 11. The continuous variation of transmitted ($T_{\max}$) and reflected intensity peaks ($R_{\max}$) with respect to change in ϕ is shown in panels (a)–(c). Panels (d) and (e) show the decrease in the peak reflectivity and transmittivity when length L of the system is increased. The changes in the FWHM of the transmitted and reflected spectra against the variation of ϕ are plotted in panel (e) and the notations FWHM$_L$ and FWHM$_R$ denote the full width half maximum of the modes on the left and right side of the 1550 nm wavelength, respectively.

3. Single-mode lasing behavior

If the phase is continuously tuned further, the secondary modes are not observed in the lasing spectra, and the reflectivity and transmittivity peaks are found to appear only in one distinct mode, as shown in Fig. 13(a). When $\phi = 270^\circ$, the lasing spectra is centered at 1549.72 nm with the FWHM of 0.008 nm is observed in the transmission as well as reflected spectra. The spectra also resemble the spectra plotted at $\phi = 90^\circ$ in terms of intensity and FWHM except for a difference that it occurs on the shorter wavelength side of the Bragg wavelength in the spectra. Any increase in the value of ϕ leads to a decrease in the reflectivity and transmittivity and increase in the FWHM as shown in Figs. 13(b) and 13(c). The wavelength over which the lasing spectrum is centered is shifted towards the Bragg wavelength as depicted in Fig. 13(c). Thus we can conclude that by carefully tuning the value of the phase shift in the middle of the grating, it is possible to control grating characteristics such as intensity, FWHM and the wavelength over which the lasing spectra is centered.

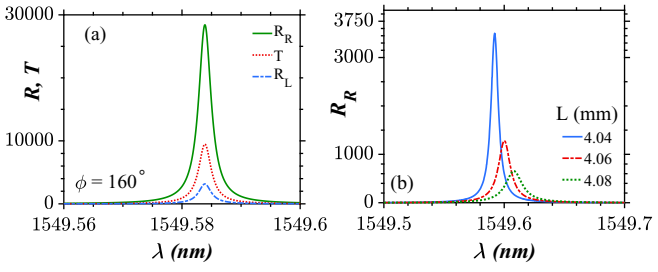

FIG. 12. Reflection and transmission spectra of a broken $\mathcal{PT}$-symmetric FBG at $g = 20$ cm^{-1} and $\phi = 160^\circ$ are shown in panel (a). Panel (b) illustrates the decrease in the peak reflectivity for the right light incidence and shift in the corresponding peak wavelengths when length L of the system is increased.

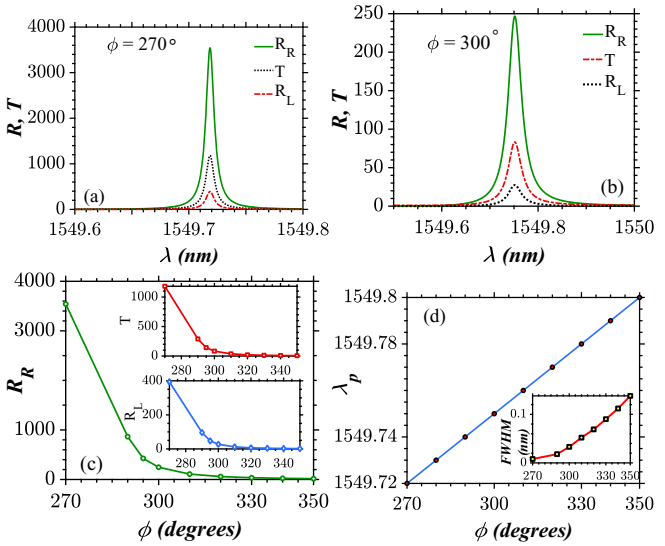

FIG. 13. (a), (b) Phase-controlled single-mode lasing behavior of a broken $\mathcal{PT}$-symmetric FBG at $g = 20$ against the variation in phase-shift values $\phi = 270^\circ$ and 300°, respectively. The continuous variation of maximum of transmittivity ($T_{\max}$) and reflectivity ($R_{\max}$) with respect to change in the values of ϕ is shown in panel (c). The wavelength λ_2 corresponding to these peaks is shown in panel (d) and the FWHM of the spectra is plotted in the inset.

IV. SPECTRAL CHARACTERISTICS OF A PPTFBG WITH MULTIPLE PHASE-SHIFT REGIONS

It is worthwhile to mention that FBGs find their main application as channel selection filters in the light wave communication systems. Investigations on improving the channels selection characteristics of FBGs are mainly targeted at increasing the width of the stopband band in the middle. However, the ranges of the stop band in practically realizable FBGs are limited. The concept of cascading multiple PTFBGs with different grating periods can give rise to a good solution to improve the transmission characteristics significantly. But it is limited by the difficulties in fabricating a compact system [65]. It should be remembered that it is possible to tailor the stop band of a $\mathcal{PT}$-symmetric FBG by introducing the concepts of chirping and apodization [32]. Furthermore, by introducing multiple phase shifts in the middle, the spacing between number of channels can be minimized without inflicting any additional penalties on the system.

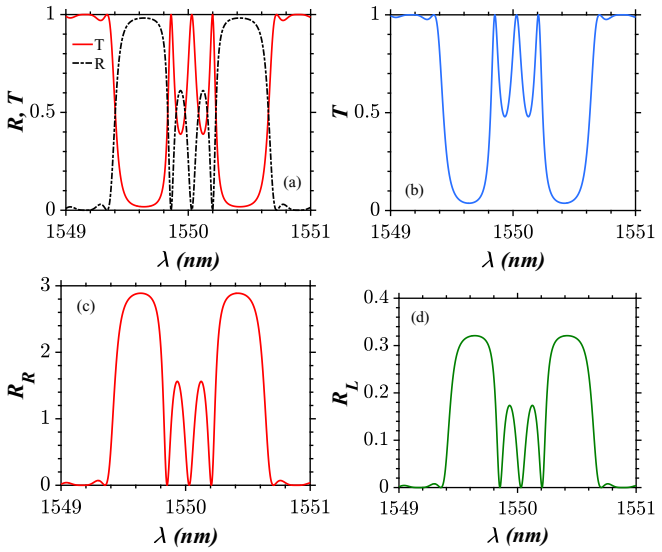

FIG. 14. (b)–(d) Reflection and transmission spectra of a unbroken PPTFBG ($g = 5$ cm^{-1}) with a phase shift ($\phi = 180^\circ$) located at $-L/4$, 0, $L/4$. Plot (a) is simulated in the absence of gain-loss ($g = 0$).

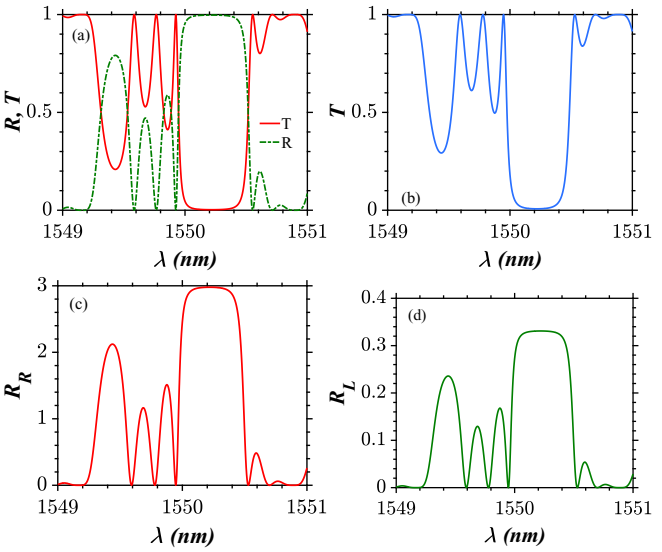

FIG. 15. (b)–(d) Reflection and transmission spectra of a unbroken PPTFBG ($g = 5$ cm^{-1}) with a phase shift ($\phi = 90^\circ$) located at $-L/4$, 0, $L/4$. Plot (a) is simulated in the absence of gain-loss ($g = 0$).

A. Unbroken $\mathcal{PT}$-symmetric regime

Figure 14 depicts the spectra of unbroken PPTFBG ($g = 5$ cm^{-1}) for an identical phase shift of $\phi = 180^\circ$ located at three locations (z_1, z_2, and z_3). Even though the locations of the phase shifts can be varied according to the requirement and thereby the position of peaks within the stopband can be controlled, we fix the location of multiple phase shifts in our investigations, as stated earlier in Sec. II. The distance between each phase-shift region is one and the same by virtue of positioning the phase shifts at $-L/4$, 0, $L/4$ along z. Finally, the reflection and transmission spectra in the presence of multiple phase shift can be found by using Eqs. (29)–(31). The number of transmission peaks and the dips in the reflectivity within the stop band is dictated by the number of phase-shift regions along the length of PPTFBG. For instance, one can find three transmission windows in Fig. 14(a) and Fig. 15(a) which are plotted in the absence of $\mathcal{PT}$ symmetry at $\phi = 180^\circ$ and $\phi = 90^\circ$, respectively. Our primary aim is to tailor the spectra by varying the magnitude of phase shift rather than varying the location of the phase shift provided that the magnitude of phase shift at all the locations is same. Also, the inclusion of $\mathcal{PT}$ symmetry paves the way to control the magnitude of the peaks which is not reported so far in the literature. It has already been proven that the usage of two or three phase-shift regions inside a conventional FBG structure is optimal for practical light wave communication systems [65]. From our investigations, we proved that the above rule of thumb holds true in the presence of gain-loss also. One of the major improvements in the spectral characteristics of the $\mathcal{PT}$-symmetric systems is that these systems open a new door toward tailoring of the spectra via an additional degree of freedom in the form of gain and loss. In Figs. 14(b)–14(d), we observe that the peaks in the middle of the stop band are symmetric in nature because the magnitude of the phase shift is $\phi = 180^\circ$. If the same system is simulated at $\phi = 90^\circ$, these multiple peaks are asymmetric and also located to the left side of the Bragg wavelength (1550 nm). Previously, we have concluded that the plots simulated at $\phi = 270^\circ$ will resemble the mirror image of the plots drawn at $\phi = 90^\circ$. This conclusion holds true even in the presence of multiple phase shifts. Like any other PTFBG system, multiple phase-shifted PTFBGs also show the directional reflection characteristics (reflectivity is different for the two light-incidence directions) and this is portrayed in Figs. 14(c), 14(d), 15(c), and 15(d). For the left incidence, the reflectivity gets decreased and it increases for the light launching condition from the other side (R_R). Thus the system enables controlling the magnitude of the peaks in two different approaches: First, by tuning the magnitude of the phase shift and alternatively by varying the value of g.

B. Exceptional-point dynamics

At the exceptional point, the phenomenon of unidirectional wave transport also remains the same as before in the present case of multiple phase shifts. This once again proves that this phenomenon relies purely on the equality between the coupling κ and gain-loss coefficient g and is independent of any variation in other control parameters, including multiple phase shifts. On the other hand, the reflection spectra for the right incidence is influenced by the presence of multiple phase shifts, i.e., their location and magnitude brings in notable changes in the spectra. We identify that there are three dips in the middle of the stop band in between two peaks on either sides for $\phi = 180^\circ$, as shown in Fig. 16(a). The same reflectivity dips are seen on the lower-wavelength (higher-wavelength) side of the Bragg wavelength when $\phi = 270^\circ$ (90°). This once again confirms that the magnitude of the phase shift is a highly influential parameter in imposing the variations in the spectra.

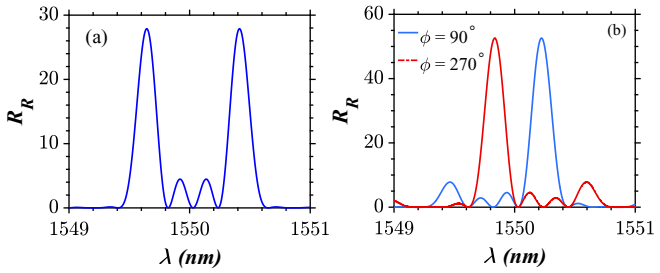

FIG. 16. Reflection (right) spectra of a PPTFBG at the exceptional point ($g = 10\ \mathrm{cm}^{-1}$) with phase shifts (equal) located at $-L/4$, 0, $L/4$. Plot (a) is simulated at $\phi = 180^\circ$ and plot (b) is simulated at $\phi = 90^\circ$ and 270°.

C. Broken $\mathcal{PT}$-symmetric regime

Previously, we interpreted that operating the system at $\phi = 180^\circ$ leads to two symmetrical reflectivity peaks on either side of the Bragg wavelength in the presence of the single phase-shift region. In the case of multiple phase shifts, there are two more symmetric reflectivity peaks closer to the Bragg wavelength whose reflectivity is comparably very less than those of the peaks far away from the Bragg wavelength, as shown in the right panels of Fig. 17. For the case $\phi = 90^\circ$, there are two reflectivity peaks observed in the left panels of Fig. 17, one with large reflectivity and the other with much less reflectivity, which is contrasting with the results obtained in the presence of the single phase-shift region, which is characterized by single-mode lasing behavior when $\phi = 90^\circ$. The results for $\phi = 270^\circ$ are simply the mirror image of plots obtained in the left panels of Fig. 17.

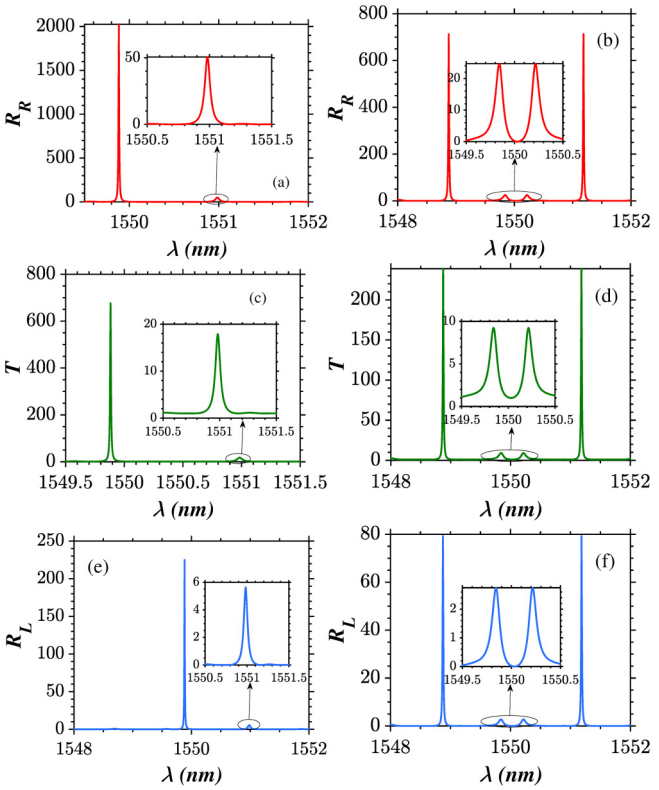

FIG. 17. Reflection and transmission spectra of a PPTFBG at the broken $\mathcal{PT}$-symmetric regime ($g = 20\ \mathrm{cm}^{-1}$) with phase shifts (equal) located at $-L/4$, 0, $L/4$. The plots in the left panels are simulated at $\phi = 90^\circ$ and the plots in the right panels are simulated at $\phi = 180^\circ$ and 270°. The top, middle, and bottom panels represent the reflection right, transmission, and reflection left spectra, respectively.

V. CONCLUSIONS

In this paper, we have analyzed the spectral characteristics of PPTFBGs in different regimes, namely, the unbroken, exceptional point, and the broken regimes. The spectral dynamics in the unbroken regime was quite similar to the spectra of a conventional phase-shifted FBG. However, we have showed that it is possible to vary the intensity of the phase-shifted spectra by varying the gain and loss parameter. Also, we made evident that the phenomenon of unidirectional reflectionless wave transport is exhibited by the proposed system. It was also shown that the device is not fully reflective within the stopband, like other PTFBG systems. However, in the presence of phase it possesses symmetrical or asymmetrical spectra about one particular wavelength, where the reflection intensity is zero inside the stopband. The broken PPTFBG was found to exhibit single-mode lasing behavior for some range of phase-shift values and dual-mode lasing behavior for the others. Also, the broken $\mathcal{PT}$-symmetric FBG system described in this work has a length of just four mm, thus making it compact. Moreover, it involves fewer discrete components to perform filtering, amplification, and side lobe suppression. We have also considered the multiple phase shifts introduced in various locations of PPTFBGs and found that they aid in controlling the number peaks in the reflection and transmission spectra. Hence it can be used to realize a narrow-band single-mode laser. The results presented here give conclusive evidence that it is possible to realize a multifunctional device which can operate as a demultiplexer and mode-selective laser from the same system configuration without a need to design a specific system for a particular application and thus simplifying the manufacturing process. We strongly believe that the fabrication of such a $\mathcal{PT}$ device(s) in the future is not too far away thanks to the current optical integration methodologies.

ACKNOWLEDGMENTS

S.V.R. is indebted to a financial assistantship provided by Anna University through an Anna Centenary Research Fellowship (CFR/ACRF-2018/AR1/24). A.G. and M.L. acknowledge the support of DST-SERB for providing a Distinguished Fellowship (Grant No. SB/DF/04/2017) to M.L. in which A.G. was a visiting scientist. A.G. is now supported by University Grants Commission (UGC), Government of India, through a Dr. D. S. Kothari Postdoctoral Fellowship (Grant No. F.4-2/2006 (BSR)/PH/19-20/0025).

[1] R. El-Ganainy, K. Makris, D. Christodoulides, and Z. H. Musslimani, Theory of coupled optical $\mathcal{PT}$-symmetric structures, Opt. Lett. **32**, 2632 (2007).

[2] T. Kottos, Optical physics: Broken symmetry makes light work, Nat. Phys. **6**, 166 (2010).

[3] C. E. Rüter, K. G. Makris, R. El-Ganainy, D. N. Christodoulides, M. Segev, and D. Kip, Observation of parity-time symmetry in optics, Nat. Phys. **6**, 192 (2010).

[4] Z. Lin, H. Ramezani, T. Eichelkraut, T. Kottos, H. Cao, and D. N. Christodoulides, Unidirectional Invisibility Induced by $\mathcal{PT}$-Symmetric Periodic Structures, Phys. Rev. Lett. **106**, 213901 (2011).

[5] L. Feng, R. El-Ganainy, and L. Ge, Non-Hermitian photonics based on parity-time symmetry, Nat. Photonics **11**, 752 (2017).

[6] R. El-Ganainy, K. G. Makris, M. Khajavikhan, Z. H. Musslimani, S. Rotter, and D. N. Christodoulides, Non-Hermitian physics and $\mathcal{PT}$-symmetry, Nat. Phys. **14**, 11 (2018).

[7] Ş. K. Özdemir, S. Rotter, F. Nori, and L. Yang, Parity-time symmetry and exceptional points in photonics, Nat. Mater. **18**, 783 (2019).

[8] A. Lupu, H. Benisty, and A. Degiron, Switching using $\mathcal{PT}$-symmetry in plasmonic systems: Positive role of the losses, Opt. Express **21**, 21651 (2013).

[9] A. Govindarajan, A. K. Sarma, and M. Lakshmanan, Tailoring $\mathcal{PT}$-symmetric soliton switch, Opt. Lett. **44**, 663 (2019).

[10] C. M. Bender and S. Boettcher, Real Spectra in Non-Hermitian Hamiltonians having $\mathcal{PT}$-Symmetry, Phys. Rev. Lett. **80**, 5243 (1998).

[11] A. Govindarajan, B. A. Malomed, and M. Lakshmanan, Nonlinear anti-directional couplers with gain and loss, Opt. Lett. **44**, 4650 (2019).

[12] A. Regensburger, C. Bersch, M.-A. Miri, G. Onishchukov, D. N. Christodoulides, and U. Peschel, Parity-time synthetic photonic lattices, Nature (London) **488**, 167 (2012).

[13] S. Phang, A. Vukovic, H. Susanto, T. M. Benson, and P. Sewell, Ultrafast optical switching using parity-time symmetric Bragg gratings, J. Opt. Soc. Am. B **30**, 2984 (2013).

[14] A. Govindarajan, B. A. Malomed, and M. Lakshmanan, Tunable nonlinear spectra of anti-directional couplers, Opt. Lett. **45**, 1918 (2020).

[15] H. Benisty, A. Lupu, and A. Degiron, Transverse periodic $\mathcal{PT}$ symmetry for modal demultiplexing in optical waveguides, Phys. Rev. A **91**, 053825 (2015).

[16] G. P. Agrawal and S. Radic, Phase-shifted fiber Bragg gratings and their application for wavelength demultiplexing, IEEE Photonics Technol. Lett. **6**, 995 (1994).

[17] T. Erdogan, Fiber grating spectra, J. Lightwave Technol. **15**, 1277 (1997).

[18] C. Giles, Lightwave applications of fiber Bragg gratings, J. Lightwave Technol. **15**, 1391 (1997).

[19] K. O. Hill and G. Meltz, Fiber Bragg grating technology fundamentals and overview, J. Lightwave Technol. **15**, 1263 (1997).

[20] A. Othonos, Fiber Bragg gratings, Rev. Sci. Instrum. **68**, 4309 (1997).

[21] H. G. Winful, J. Marburger, and E. Garmire, Theory of bistability in nonlinear distributed feedback structures, Appl. Phys. Lett. **35**, 379 (1979).

[22] S. Radic, N. George, and G. P. Agrawal, Theory of low-threshold optical switching in nonlinear phase-shifted periodic structures, J. Opt. Soc. Am. B **12**, 671 (1995).

[23] E. Yousefi, M. Hatami, and A. T. Jahromi, All-optical ternary signal processing using uniform nonlinear chalcogenide fiber Bragg gratings, J. Opt. Soc. Am. B **32**, 1471 (2015).

[24] K. Hill, Y. Fujii, D. C. Johnson, and B. Kawasaki, Photosensitivity in optical fiber waveguides: Application to reflection filter fabrication, Appl. Phys. Lett. **32**, 647 (1978).

[25] G. Meltz, W. Morey, and W. Glenn, Formation of Bragg gratings in optical fibers by a transverse holographic method, Opt. Lett. **14**, 823 (1989).

[26] M. Karimi, M. Lafouti, A. A. Amidiyan, and J. Sabbaghzadeh, All-optical flip-flop based on nonlinear effects in fiber Bragg gratings, Appl. Opt. **51**, 21 (2012).

[27] N. Broderick, Bistable switching in nonlinear Bragg gratings, Opt. Commun. **148**, 90 (1998).

[28] H. G. Winful and V. Perlin, Raman Gap Solitons, Phys. Rev. Lett. **84**, 3586 (2000).

[29] D. Mills and S. Trullinger, Gap solitons in nonlinear periodic structures, Phys. Rev. B **36**, 947 (1987).

[30] C. M. De Sterke and J. Sipe, Switching dynamics of finite periodic nonlinear media: A numerical study, Phys. Rev. A **42**, 2858 (1990).

[31] S. V. Raja, A. Govindarajan, A. Mahalingam, and M. Lakshmanan, Multifaceted dynamics and gap solitons in $\mathcal{PT}$-symmetric periodic structures, Phys. Rev. A **100**, 033838 (2019).

[32] S. V. Raja, A. Govindarajan, A. Mahalingam, and M. Lakshmanan, Tailoring inhomogeneous $\mathcal{PT}$-symmetric fiber-Bragg-grating spectra, Phys. Rev. A **101**, 033814 (2020).

[33] S. Radic, N. George, and G. P. Agrawal, Optical switching in $\lambda/4$-shifted nonlinear periodic structures, Opt. Lett. **19**, 1789 (1994).

[34] A. Melloni, M. Chinello, and M. Martinelli, All-optical switching in phase-shifted fiber Bragg grating, IEEE Photonics Technol. Lett. **12**, 42 (2000).

[35] A. Suryanto, On the numerical modeling of optical-switching in non-linear phase-shifted grating, J. Nonlinear Opt. Phys. Mater. **18**, 129 (2009).

[36] X. Liu, X. Shu, and H. Cao, Proposal of a phase-shift fiber Bragg grating as an optical differentiator and an optical integrator simultaneously, IEEE Photonics J. **10**, 7800907 (2018).

[37] M. Kulishov, J. M. Laniel, N. Bélanger, J. Azaña, and D. V. Plant, Nonreciprocal waveguide Bragg gratings, Opt. Express **13**, 3068 (2005).

[38] S. Longhi, Optical Realization of Relativistic Non-Hermitian Quantum Mechanics, Phys. Rev. Lett. **105**, 013903 (2010).

[39] S. Longhi, $\mathcal{PT}$-symmetric laser absorber, Phys. Rev. A **82**, 031801 (2010).

[40] C. Huang, R. Zhang, J. Han, J. Zheng, and J. Xu, Type-II perfect absorption and amplification modes with controllable bandwidth in combined $\mathcal{PT}$-symmetric and conventional Bragg grating structures, Phys. Rev. A **89**, 023842 (2014).

[41] S. Longhi, Supersymmetric Bragg gratings, J. Opt. (Bristol, U. K.) **17**, 045803 (2015).

[42] A. T. Lupu, H. Benisty, and A. V. Lavrinenko, Tailoring spectral properties of binary $\mathcal{PT}$-symmetric gratings by duty-cycle methods, IEEE J. Sel. Top. Quantum Electron. **22**, 35 (2016).

[43] F. Correa and V. Jakubský, Confluent Crum-Darboux transformations in Dirac Hamiltonians with $\mathcal{PT}$-symmetric Bragg gratings, Phys. Rev. A **95**, 033807 (2017).

[44] J. Sun, X. Yuan, X. Zhang, and D. Huang, Single-longitudinal-mode fiber ring laser using fiber grating-based Fabry-Pérot filters and variable saturable absorbers, Opt. Commun. **267**, 177 (2006).

[45] X. Cheng, P. Shum, C. Tse, J. Zhou, M. Tang, W. Tan, R. Wu, and J. Zhang, Single-longitudinal-mode erbium-doped fiber ring laser based on high finesse fiber Bragg grating Fabry-Pérot etalon, IEEE Photonics Technol. Lett. **20**, 976 (2008).

[46] X. He, X. Fang, C. Liao, D. Wang, and J. Sun, A tunable and switchable single-longitudinal-mode dual-wavelength fiber laser with a simple linear cavity, Opt. Express **17**, 21773 (2009).

[47] S. Feng, O. Xu, S. Lu, T. Ning, and S. Jian, Switchable single-longitudinal-mode dual-wavelength erbium-doped fiber ring laser based on one polarization-maintaining fiber Bragg grating incorporating saturable absorber and feedback fiber loop, Opt. Commun. **282**, 2165 (2009).

[48] S. Pan and J. Yao, A wavelength-tunable single-longitudinal-mode fiber ring laser with a large sidemode suppression and improved stability, IEEE Photonics Technol. Lett. **22**, 413 (2010).

[49] K. Hill, F. Bilodeau, B. Malo, T. Kitagawa, S. Theriault, D. Johnson, J. Albert, and K. Takiguchi, Chirped in-fiber Bragg gratings for compensation of optical-fiber dispersion, Opt. Lett. **19**, 1314 (1994).

[50] K. Ennser, N. Zervas, and R. Laming, Optimization of apodized linearly chirped fiber gratings for optical communications, IEEE J. Quantum Electron. **34**, 770 (1998).

[51] D. Pastor, J. Capmany, D. Ortega, V. Tatay, and J. Martí, Design of apodized linearly chirped fiber gratings for dispersion compensation, J. Lightwave Technol. **14**, 2581 (1996).

[52] A. K. Sarma, Modulation instability in nonlinear complex parity-time symmetric periodic structures, J. Opt. Soc. Am. B **31**, 1861 (2014).

[53] M.-A. Miri, A. B. Aceves, T. Kottos, V. Kovanis, and D. N. Christodoulides, Bragg solitons in nonlinear $\mathcal{PT}$-symmetric periodic potentials, Phys. Rev. A **86**, 033801 (2012).

[54] A. Cusano, D. Paladino, and A. Iadicicco, Microstructured fiber Bragg gratings, J. Lightwave Technol. **27**, 1663 (2009).

[55] W. Loh, M. Cole, M. N. Zervas, S. Barcelos, and R. Laming, Complex grating structures with uniform phase masks based on the moving fiber-scanning beam technique, Opt. Lett. **20**, 2051 (1995).

[56] L. Xia, P. Shum, and C. Lu, Phase-shifted bandpass filter fabrication through CO_2 laser irradiation, Opt. Express **13**, 5878 (2005).

[57] S. Rota-Rodrigo, L. Rodríguez-Cobo, M. Á. Quintela, J. M. López-Higuera, and M. López-Amo, Dual-wavelength single-longitudinal mode fiber laser using phase-shift Bragg gratings, IEEE J. Sel. Top. Quantum Electron. **20**, 161 (2013).

[58] S. Legoubin, E. Fertein, M. Douay, P. Bernage, P. Niay, F. Bayon, and T. Georges, Formation of Moiré grating in core of germanosilicate fibre by transverse holographic double exposure method, Electron. Lett. **27**, 1945 (1991).

[59] E. Chehura, S. W. James, and R. P. Tatam, A simple and wavelength-flexible procedure for fabricating phase-shifted fibre Bragg gratings, Meas. Sci. Technol. **21**, 094001 (2010).

[60] C. Liao, L. Xu, C. Wang, D. Wang, Y. Wang, Q. Wang, K. Yang, Z. Li, X. Zhong, J. Zhou *et al.*, Tunable phase-shifted fiber Bragg grating based on femtosecond laser fabricated in-grating bubble, Opt. Lett. **38**, 4473 (2013).

[61] X. Chen, Y. Painchaud, K. Ogusu, and H. Li, Phase shifts induced by the piezoelectric transducers attached to a linearly chirped fiber Bragg grating, J. Lightwave Technol. **28**, 2017 (2010).

[62] M. Janos and J. Canning, Permanent and transient resonances thermally induced in optical fibre Bragg gratings, Electron. Lett. **31**, 1007 (1995).

[63] A. A. S. Falah, M. R. Mokhtar, Z. Yusoff, and M. Ibsen, Reconfigurable phase-shifted fiber Bragg grating using localized micro-strain, IEEE Photonics Technol. Lett. **28**, 951 (2016).

[64] J. Zhou, K. Guo, J. He, M. Hou, Z. Zhang, C. Liao, Y. Wang, G. Xu, and Y. Wang, Novel fabrication technique for phase-shifted fiber Bragg gratings using a variable-velocity scanning beam and a shielded phase mask, Opt. Express **26**, 13311 (2018).

[65] R. Zengerle and O. Leminger, Phase-shifted Bragg-grating filters with improved transmission characteristics, J. Lightwave Technol. **13**, 2354 (1995).